



Formation of quasi-core-shell In_2S_3 /anatase TiO_2 @metallic $\text{Ti}_3\text{C}_2\text{T}_x$ hybrids with favorable charge transfer channels for excellent visible-light-photocatalytic performance



Hou Wang^{a,b}, Yan Wu^a, Tong Xiao^a, Xingzhong Yuan^b, Guangming Zeng^b, Wenguang Tu^a, Shuyang Wu^a, Heng Yeong Lee^c, Yong Zen Tan^a, Jia Wei Chew^{a,d,*}

^a School of Chemical and Biomedical Engineering, Nanyang Technological University, Singapore, 637459, Singapore

^b College of Environmental Science and Engineering, Hunan University, Changsha, 410082, PR China

^c School of Materials Science and Engineering, Nanyang Technological University, Singapore, 639798, Singapore

^d Singapore Membrane Technology Center, Nanyang Environment and Water Research Institute, Nanyang Technological University, Singapore, 639798, Singapore

ARTICLE INFO

Keywords:

Indium sulfide
MXene
Heterojunction
Photocatalysis
Charge transfer channels

ABSTRACT

Semiconductor-based heterojunctions, widely applied in photocatalytic solar-to-chemical energy conversion, are advantageous for synergistically expediting photocatalytic reaction beyond individual the constituent components. Here we showed new quasi-core-shell In_2S_3 /anatase TiO_2 @metallic $\text{Ti}_3\text{C}_2\text{T}_x$ hybrids consisting of well-designed type-II heterojunction and non-noble metal-based Schottky junction with favorable charge transfer channels for efficient photocatalysis application. The mesoporous hybrids owned pleasurable visible-light absorption property and excellent capability in photogenerated exciton separation and carrier transport. Specifically, the hybridized photocatalyst with the additive $\text{Ti}_3\text{C}_2\text{T}_x$ content of 16 mg (InTi-16) had excellent visible-light photocatalytic performance towards pollutant removal in water with a degradation rate of 0.04977 min^{-1} , which was 3.2 and 6.2 folds higher than that of pure In_2S_3 and pure $\text{Ti}_3\text{C}_2\text{T}_x$, respectively. What's more, the photocatalytic degradation ability of InTi-16 had surpassed that of many other types of In_2S_3 -based photocatalyst including In_2S_3 /carbon nanotube (CNT), In_2S_3 /reduced graphene oxide (rGO), $\text{In}_2\text{S}_3/\text{MoS}_2$, and $\text{In}_2\text{S}_3/\text{TiO}_2$ hybrids. The promising photocatalytic performance was strongly depended on the separation and diffusion of photogenerated exciton and carrier via a multitude of charge transfer channels due to the formation of double heterostructure (type-II heterojunction and Schottky junction). It had originated from the synergistic effects among the visible-light absorption of In_2S_3 , the upward band bending of TiO_2 and the favorable electrical conductivity of $\text{Ti}_3\text{C}_2\text{T}_x$. Prolonger electron lifetime favored for the generation of more strongly oxidizing radical (e.g. $\cdot\text{O}_2^-$) at the in-plane of $\text{Ti}_3\text{C}_2\text{T}_x$, and thus enhanced photocatalytic degradation ability. This work demonstrates that the $\text{TiO}_2/\text{Ti}_3\text{C}_2\text{T}_x$ can be a potentially novel platform for constructing efficient photocatalysts both for wide-ranging applications and unraveling the transfer behavior of photo-excited electrons based on charge transfer channels.

1. Introduction

With regards to the harvesting and conversion of solar energy for addressing issues on the environment and sustainable energy, photocatalysis is considered as the most promising approach [1–4]. The boom of two-dimensional (2D) materials has tremendous impact on both fundamental studies and practical applications in photocatalytic fields [5–7]. Numerous kinds of 2D materials have been developed including single-element material (e.g., graphene, phosphorene), the more popular two-element materials (e.g., hexagonal boron nitride, transition

metal dichalcogenides, carbon nitride, and the multi-element ones (e.g., metal organic frameworks and covalent organic frameworks) [8–16]. Transition metal carbides/carbonitrides/nitrides, known as MXene, are the latest group of layer-structure materials with the metal-carbon and/or nitrogen host layer decorated with or without functional groups in surface termination [17–19]. MXene has many unique properties such as metallic conductivity (or transition phase), tunable band gap structure, anisotropic behavior of carrier mobility, layer-dependent optical transparency and absorption, etc [20–22]. These features offer attractive platforms for practical applications in electrochemical devices (e.g.

* Corresponding author at: School of Chemical and Biomedical Engineering, Nanyang Technological University, Singapore, 637459, Singapore.
E-mail addresses: JChew@ntu.edu.sg, chewj@colorado.edu (J.W. Chew).

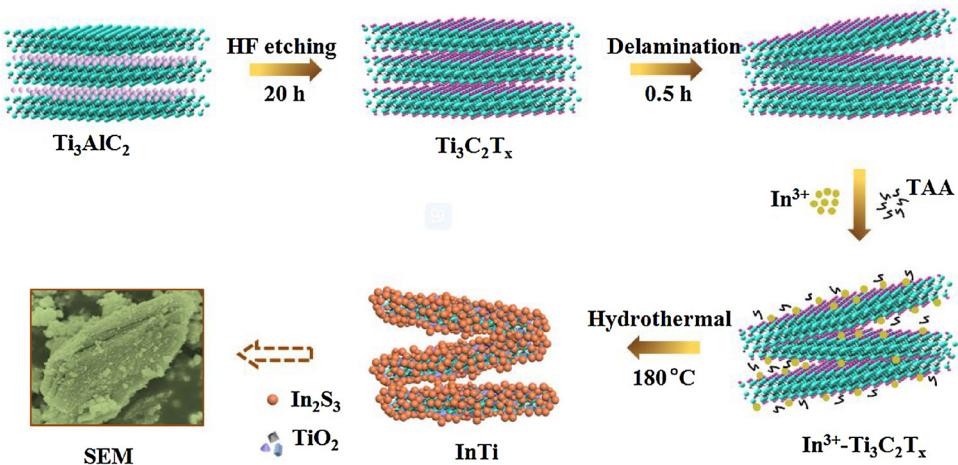


Fig. 1. Illustration of the synthesis process for the $\text{In}_2\text{S}_3/\text{Ti}_3\text{C}_2\text{T}_x$ hybrids.

supercapacitor, battery), catalysis, membrane separation, adsorption, sensor and cellular imaging [20,23–29].

Specifically for the photocatalysis, several outstanding characteristics of MXene are highlighted as follows: (i) the high anisotropic carrier (electron and hole) mobility in MXene systems facilitates the migration and separation of photogenerated electron–hole pairs [30]; (ii) part of MXene ($M_2\text{CT}_x$, $M = \text{Ti}$, Zr , and Hf) have the band gap in the range of 0.92–1.75 eV with good light absorbance [31,32]. The band gap structure can be further adjusted by altering their surface chemistries (e.g. the terminated $-\text{F}$, $-\text{OH}$, or $-\text{O}$ groups) or the arrangements of surface groups; and (iii) MXene, used as a supporter, alters the electrophilicity of the active centers of the catalysts due to the ultralow work function, excellent electrical conductivity ($6.76 \times 10^5 \text{ S/m}$) and electronegative surface [33,34]. Recently, Mashtalar et al. was one of the first who observed that $\text{Ti}_3\text{C}_2\text{T}_x$ degraded methylene blue and acid blue 80 with degradation efficiencies of 81% and 62%, respectively, upon ultraviolet (UV) irradiation over 5 h [35]. The $\text{Ti}_3\text{C}_2\text{T}_x$ has been used to in situ prepare the $\text{Ti}_3\text{C}_2\text{T}_x/\text{TiO}_2$ composite for enhancing the UV-driven photocatalytic performance by serving as a reservoir of holes to promote the carrier transport of TiO_2 via the interfacial Schottky junction [36–39]. Compared with the pure TiO_2 , the photoinduced electron lifetime can be prolonged almost two orders-of-magnitude due to the heterojunctions formed between TiO_2 nanosheets and layered Ti_3C_2 [36]. Ran et al. used Ti_3C_2 nanoparticles as the co-catalyst to investigate the improved photocatalytic activity of cadmium sulfide in H_2 production [24]. The hybrid induced a visible-light photocatalytic hydrogen production activity of $14,342 \text{ mmol h}^{-1} \text{ g}^{-1}$ with an apparent quantum efficiency of 40.1% at 420 nm. These favorable phenomena inspire the design of MXene-based nanoarchitectures to increase the light harvesting ability, attain greater quantum efficiency and enhance the exciton separation with superior photoredox applications.

Metal sulfides, a major group of abundant and cheap minerals such as greenockite (CdS), berndtite (SnS_2), stibnite (Sb_2S_3), heazlewoodite (Ni_3S_2), chalcocite (Cu_2S), pyrite (FeS_2), and so on, have been demonstrated as visible-light-responsive photocatalysts for energy conversion and environmental remediation [40–42]. Indium (III) sulfide (In_2S_3) with various morphologies including nanoplates, nanotubes, hollow microspheres and nanorods have garnered significant attention because of good photosensitivity, stable physicochemical characteristics and low toxicity. For instance, Gao et al. reported that tetragonal In_2S_3 nanoparticles, with irregular morphology and particle size of 5–20 nm, displayed photocatalytic degradation abilities for pollutants under UV, visible light and near-infrared light [43]. Li et al. synthesized the carbon quantum dots@3D daisy-like $\text{In}_2\text{S}_3/\text{single-wall carbon nanotube}$ with fast electron transfer and enhanced visible light

photocatalytic pollutant degradation [44]. Our previous research also showed that the core-shell $\text{In}_2\text{S}_3@\text{MIL}-125(\text{Ti})$ heterojunction could remove tetracycline from wastewater by visible-light-driven photocatalysis, ascribing to the open porous structure, effective transfer of photo-generated carriers, $\text{Ti}^{3+}-\text{Ti}^{4+}$ intervalence electron transfer and the synergistic effect between $\text{MIL}-125(\text{Ti})$ and In_2S_3 [45]. Similar core-shell catalysts with enhanced performance have also been developed in the photocatalysis field [46–50]. However, reducing the recombination of photogenerated electro-hole pairs still remains the key challenge in further enhancing photocatalytic activity.

In_2S_3 can serve as an efficient sensitizer for non-visible-light-responsive catalysts to capture more solar energy. Compared to the binary heterostructure, In_2S_3 -based ternary heterostructured photocatalysts with suitable and gradual alteration in energy band are more favorable to satisfy the demand for high-efficiency photocatalysts. Among these, the designed heterostructure, including type-II staggered band alignment heterojunctions and Schottky junction between two components, enables the inhibition of the charge recombination process. In the presence of the Schottky barrier, single-direction-transfer route is enabled to make the electrons only transfer from the semiconductor to the metal surface. Because the reduction reaction occurs more readily on the surface of metallic materials than on that of the semiconductor, these synergistic double-heterojunctions serve as favorable charge transfer channels for the photogenerated electron separation and transfer. In view of the low cost and metallic features, $\text{Ti}_3\text{C}_2\text{T}_x$ is a promising material to simultaneously construct In_2S_3 -based dual-heterostructure photocatalyst via one-step synthesis routes. The question that has yet been addressed is whether the $\text{Ti}_3\text{C}_2\text{T}_x$ and partly derived TiO_2 can simultaneously serve as the new platform to improve the photoelectrochemical properties of the semiconductor photocatalyst when used for photocatalysis. Also, it is important from an academic perspective to unravel the transfer behavior of photo-excited electrons based on charge transfer channels in order to contribute towards the understanding on the electronic properties of photocatalysts for developing more efficient hybrid systems.

In this study, novel quasi-core-shell $\text{In}_2\text{S}_3/\text{anatase TiO}_2@\text{metallic Ti}_3\text{C}_2\text{T}_x$ MXene heterostructured hybrids were prepared by a facile in situ hydrothermal method (Fig. 1). The morphology, structure, surface chemical state and photo-electrochemical properties were investigated by various characterization techniques. With the aid of charge transfer channels in the heterostructured interface (type-II heterojunction and Schottky junction) among the In_2S_3 , anatase TiO_2 and metallic $\text{Ti}_3\text{C}_2\text{T}_x$, the hybrids were found to exhibit superior photocatalytic performance towards pollutant degradation under visible light irradiation. Results showed that the photocatalytic capability of the $\text{In}_2\text{S}_3/\text{TiO}_2@\text{Ti}_3\text{C}_2\text{T}_x$ hybrids was better than that of $\text{In}_2\text{S}_3/\text{CNT}$, $\text{In}_2\text{S}_3/\text{rGO}$, $\text{In}_2\text{S}_3/\text{MoS}_2$ and

$\text{In}_2\text{S}_3/\text{TiO}_2$ under the same conditions. The mechanism underlying the enhanced photocatalytic performance was also explored, which indicate that the $\text{Ti}_3\text{C}_2\text{T}_x$ combined with derived TiO_2 can be potentially applied for photocatalysis in various applications.

2. Experimental

2.1. Materials

All reagents and solvents were of analytical reagent grade and used as received from commercial suppliers. $\text{Ti}_3\text{C}_2\text{T}_x$ MXene was synthesized according to the procedures reported by Naguib et al. [51] with minor modifications. Briefly, 1 g of Ti_3AlC_2 powders were slowly added into 50% hydrogen fluoride (10 mL) and immersed for 20 h. The resulting black suspension was then centrifuged to separate the powders and washed six times using deoxygenated deionized water until the pH of the supernatant was approximately 6. Finally, the black $\text{Ti}_3\text{C}_2\text{T}_x$ solid was obtained after drying at 60 °C under vacuum for 12 h.

2.2. Synthesis of $\text{In}_2\text{S}_3/\text{TiO}_2@\text{Ti}_3\text{C}_2\text{T}_x$ hybrids and other In_2S_3 -based photocatalyst

1 mmol $\text{In}(\text{NO}_3)_3 \cdot x\text{H}_2\text{O}$ and 3 mmol thioacetamide (CH_3CSNH_2 , TAA) was dissolved into 20 mL deoxygenated deionized water to form a clear solution. Then, 10 mL of black $\text{Ti}_3\text{C}_2\text{T}_x$ dispersed in aqueous solution with the targeted amount of $\text{Ti}_3\text{C}_2\text{T}_x$ was added into the above clear solution and stirred for 2 h under the protection of argon gas. The mixture was subjected to hydrothermal conditions in a Teflon-lined stainless-steel autoclave at 180 °C for 24 h. After reaction, the deep yellow precipitate was separated by centrifugation and washed with deionized water. By drying in a vacuum oven at 60 °C, the final products were collected for further characterization and experiments. In order to obtain various ratios of In_2S_3 to $\text{TiO}_2/\text{Ti}_3\text{C}_2\text{T}_x$, the mass of $\text{Ti}_3\text{C}_2\text{T}_x$ added during the synthesis process was 8 mg, 16 mg, 32 mg or 54 mg, the as-obtained hybrids of which were denoted InTi-8, InTi-16, InTi-32 and InTi-54. The mass ratio of In_2S_3 to $(\text{TiO}_2/\text{Ti}_3\text{C}_2\text{T}_x)$ in InTi-8, InTi-16, InTi-32 and InTi-54 hybrids were estimated to about 1:0.062, 1:0.123, 1:0.246 and 1:0.415, respectively. The synthesis process is illustrated in Fig. 1. For comparison purposes, conventional In_2S_3 was prepared in the absence of $\text{Ti}_3\text{C}_2\text{T}_x$ under the same condition. The $\text{TiO}_2/\text{Ti}_3\text{C}_2\text{T}_x$ composites were also synthesized without In^{3+} and TAA under the hydrothermal temperatures of 150 °C, 180 °C and 200 °C.

For the preparation of In_2S_3 -based materials, the same procedures as with the synthesis of $\text{In}_2\text{S}_3/\text{TiO}_2@\text{Ti}_3\text{C}_2\text{T}_x$ hybrids were carried out. But the $\text{Ti}_3\text{C}_2\text{T}_x$ was substituted by 16 mg of either pure titanium dioxide (TiO_2) nanoparticles, reduced graphene oxide (rGO), carbon nanotube (CNT) or molybdenum disulfide (MoS_2).

2.3. Analytical method

The powder X-ray diffraction (XRD) patterns were recorded using Bruker D2-Phaser XRD diffractometer to investigate the crystal structure of photocatalyst. The morphologies of as-obtained samples were characterized by a field emission scanning electron microscopy and transmission electron microscopy. Surface electronic state was measured by X-ray photoelectron spectroscopy. Nitrogen adsorption-desorption performance of photocatalyst was tested to characterize the specific surface area and porous distribution. UV-vis diffuse-reflectance spectra (UV-vis DRS) were scanned in the range of 200–800 nm with a UV-2250 spectrometer equipped with an integrating sphere. Photoluminescence (PL) spectroscopy was recorded via the Perkin-Elmer LS-55 spectrofluorimeter at room temperature. The time-resolved fluorescence decay spectrum was measured by Edinburgh FLS980 spectrophotometer under the given excitation wavelength. The electron spin resonance (ESR) signals of radicals spin-trapped by spin-trapped reagent 5, 5-dimethyl-l-pyrroline N-oxide (DMPO) and 2,2,6,6-

Tetramethylpiperidinoxy (TEMPO) were examined under the light spectrum range of $\lambda > 420$ nm. All the experiments were operated in darkness and also visible light irradiation durations of 5 min, 10 min and 15 min. The transient photocurrent (TPC) response and electrochemical impedance spectra (EIS) were measured via a CHI 660C electrochemical station in a standard three electrode configuration. The total organic carbon (TOC) in water after photocatalytic process was measured using a Shimadzu TOC-VCPh analyzer. The qualitative detection of degradation intermediates was performed by high performance liquid chromatography - mass spectrometer (HPLC-MS). The mobile-phase was acetonitrile/water (60/40, v/v) at a flow rate of 0.4 mL/min. The column temperature was kept at 30 °C and injection volume was 10 µL. Thermalgravimetric (TG) data was collected in the Thermal Gravimetric Analyser (Netzsch 409C TGA PerkinElmer).

2.4. Evaluation of photocatalytic performance

Methyl orange (MO) was chosen as a target pollutant. Photocatalytic degradation of MO was carried out in a 250 mL beaker containing 100 mL MO solution (20 mg L⁻¹) and 60 mg photocatalyst. After getting the adsorption-desorption equilibrium in a darkroom, the solution was then irradiated under visible-light illumination ($\lambda > 420$ nm). A 300 W Xenon lamp (Beijing China Education Au-light, Co., Ltd.) with a 420 nm cutoff filter was used as the visible-light source. The light intensity of the 300 W Xenon lamp was 300 mW cm⁻². At time intervals, a certain amount of liquid was withdrawn and centrifuged at 10,000 rpm for 5 min to remove the residue particles. The residual MO concentration was measured using a UV-vis spectrophotometer (UV-2250, SHIMADZU Corporation, Japan) at the wavelength of 463 nm.

3. Results and discussion

3.1. Crystal structure and morphology

The X-ray diffraction patterns of Ti_3AlC_2 , $\text{Ti}_3\text{C}_2\text{T}_x$ and $\text{Ti}_3\text{C}_2\text{T}_x\text{-180}$ are presented in Fig. 2. After Ti_3AlC_2 was etched by HF, the diffraction peaks at 9.2°, 18.4°, 27.7°, 34.6°, 42.0° and 60.9° correspond to the (002), (004), (006), (101), (105) and (110) reflection of $\text{Ti}_3\text{C}_2\text{T}_x$ [52]. Compared with $\text{Ti}_3\text{C}_2\text{T}_x$, the (002) at 9.9° and (004) at 19.5° of Ti_3AlC_2 are broadened and shifted toward lower angle side, indicating the removal of interlayer Al and the formation of $\text{Ti}_3\text{C}_2\text{T}_x$ nanosheets [53]. Upon the hydrothermal oxidation, new peaks appear at 25.6°, 38.1°, 54.1° and 55.2°, demonstrating the emergence of anatase TiO_2 phase (JCPDS No. 21-1272) [37]. For InTi hybrids with different amounts of $\text{Ti}_3\text{C}_2\text{T}_x$, the XRD patterns are the characteristic peaks of In_2S_3 . The peaks located at $2\theta = 14.5^\circ$, 28.2°, 34.0°, 44.0° and 48.3° are distinctly indexed respectively to the (111), (311), (400), (511), and (440) crystal planes of cubic In_2S_3 phase structure ($\beta\text{-In}_2\text{S}_3$) (JCPDS 32-0456) [54]. The crystal structure is shown in Fig. S1 in Supporting information. Compared to the XRD patterns of pure In_2S_3 , some new peaks at 25.6°, 38.1°, 54.1° and 55.2° appeared in the InTi hybrids, corresponding to the (101), (112), (105) and (211) planes in anatase TiO_2 . Meanwhile, the content of anatase TiO_2 increased as the composition of $\text{Ti}_3\text{C}_2\text{T}_x$. The disappearance of the peak corresponding to $\text{Ti}_3\text{C}_2\text{T}_x$ is ascribed to the small amount and relatively low diffraction intensity of $\text{Ti}_3\text{C}_2\text{T}_x$ in contrast to In_2S_3 and TiO_2 . Moreover, based on molybdenum disulfide and carbon nitride, the majority of catalytically active sites are confined to the edges, while the in-plane atoms are catalytically inert [55]. From Fig. 2, the layered structures of $\text{Ti}_3\text{C}_2\text{T}_x$ might be damaged since a large amount of irregular In_2S_3 nanoparticles were on the surface and interlayer of the $\text{Ti}_3\text{C}_2\text{T}_x$ nanosheets. 2D $\text{Ti}_3\text{C}_2\text{T}_x$ with excellent charge transfer kinetics still had adequate catalytic sites, specifically, active non-edge atoms. The changed structures, ranging from multi-layer, few-layer to even single layer, are advantageous for exposing more active sites of $\text{Ti}_3\text{C}_2\text{T}_x$, facilitating the rapid electron transfer between

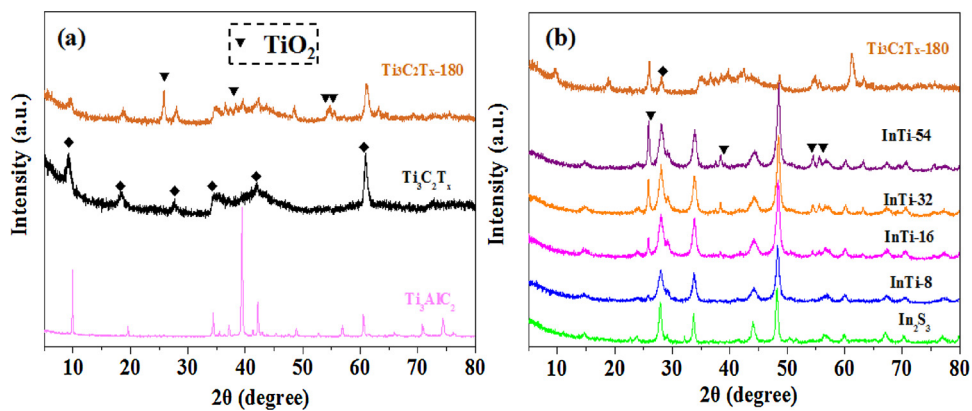
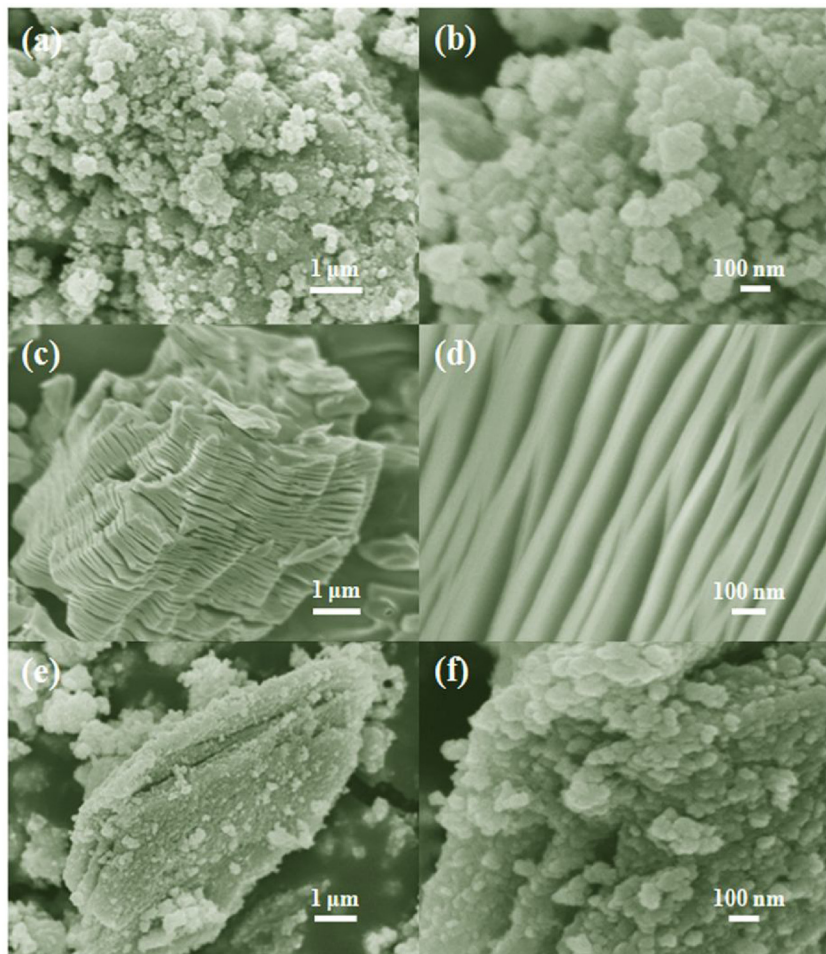


Fig. 2. XRD patterns of as-obtained photocatalysts.

electrolyte and active materials [56,57]. Thus, the modulated structures lead to the formation of In₂S₃/anatase TiO₂@metallic Ti₃C₂T_x hybrids with more favorable charge transfer channels.

The texture of In₂S₃, Ti₃C₂T_x, InTi-16, Ti₃C₂T_x-150, Ti₃C₂T_x-180 and Ti₃C₂T_x-200 samples observed via FESEM are presented in Fig. 3 and Fig. S2. It is shown that the In₂S₃ are the irregular nanoparticles with particle sizes in the range of 50~80 nm (Fig. 3a and b). Figs. 3c and d indicate that the Ti₃C₂T_x exhibited a layered morphology with each layer having a thickness of ~60 nm. Such layered and interconnected structure provides abundant open channels advantageous to the transport and diffusion of ions. The Ti₃C₂T_x nanosheets with negative charge

have hydrophilic surface and many terminated functional groups (i.e. –OH, –O or –F) [17,19]. As shown in Fig. 1, after the addition of In³⁺ ions, the Ti₃C₂T_x nanosheets served as an adsorbent for the immobilization of In³⁺ cations in aqueous solution. The In³⁺ ions can be adsorbed near the edges of multilayer hydrophilic Ti₃C₂T_x, and also diffuse into the deeper sites since the interior of particles has been reported to have favorable activation energies for In³⁺ ions adsorption and intercalation [19,58]. During the hydrothermal reaction in the presence of In³⁺ and thioacetamide, the S²⁻ anions react with the adsorbed In³⁺, inducing the heterogeneous nucleation and growth of In₂S₃ nanoparticles. Consequently, a large amount of irregular In₂S₃

Fig. 3. FESEM images of (a, b) In₂S₃, (c,d) Ti₃C₂T_x and InTi-16.

nanoparticles grow on the edge and surface of $\text{Ti}_3\text{C}_2\text{T}_x$ nanosheets (Fig. 3e and f).

Meanwhile, the $-\text{F}$ terminations may be replaced by $-\text{O}$ and $-\text{OH}$ in the water environment and TiO_2 nanoparticles formed as by-products due to the defects of Ti_3C_2 . For comparison, $\text{Ti}_3\text{C}_2\text{T}_x$ was treated in the absence of In^{3+} and thioacetamide under the hydrothermal temperatures of 150 °C, 180 °C and 200 °C. Fig. S2 shows that a mass of densely packed and irregularly shaped nanoparticles appeared on the surface or edges of $\text{Ti}_3\text{C}_2\text{T}_x$. Based on XRD results, these nanoparticles should be anatase titanium dioxide crystal due to the partial oxidation of $\text{Ti}_3\text{C}_2\text{T}_x$ [35]. With the increase of temperature, the amount of TiO_2 nanoparticles increased and even enfolded $\text{Ti}_3\text{C}_2\text{T}_x$, damaging the layer structure of $\text{Ti}_3\text{C}_2\text{T}_x$ more seriously by the simultaneous growth of In_2S_3 nanoparticles and TiO_2 crystals.

In previous studies, the chemical formula of pristine $\text{Ti}_3\text{C}_2\text{T}_x$ is usually expressed as $\text{Ti}_3\text{C}_2(\text{OH})\text{F}_{0.5}$ [37,39]. So the contents of $\text{Ti}_3\text{C}_2(\text{OH})\text{F}_{0.5}$ and formed rutile TiO_2 can be estimated by the increment of weight in thermogravimetric analysis (TGA). The mass fraction of $\text{Ti}_3\text{C}_2(\text{OH})\text{F}_{0.5}$ in composites was calculated by the following equation [39]:

$$W = \frac{W_1}{W_0}$$

where W is the fraction of $\text{Ti}_3\text{C}_2(\text{OH})\text{F}_{0.5}$ in the $\text{TiO}_2/\text{Ti}_3\text{C}_2\text{T}_x$ composites, W_1 is the increment of weight of $\text{TiO}_2/\text{Ti}_3\text{C}_2\text{T}_x$ composites, and W_0 is the increment of weight of pristine $\text{Ti}_3\text{C}_2(\text{OH})\text{F}_{0.5}$. As shown in Fig. S3, the W_0 and W_1 values were 7.987% and 1.446%, respectively. The mass fraction of $\text{Ti}_3\text{C}_2(\text{OH})\text{F}_{0.5}$ (or $\text{Ti}_3\text{C}_2\text{T}_x$) in $\text{TiO}_2/\text{Ti}_3\text{C}_2\text{T}_x$ composites under the hydrothermal temperature of 180 °C was estimated to be 18.104%. Therefore, the ratio of $\text{Ti}_3\text{C}_2\text{T}_x$ and TiO_2 in the $\text{TiO}_2/\text{Ti}_3\text{C}_2\text{T}_x$ was about 1: 4.523. As for InTi-16 with the mass ratio of 1:0.123 in In_2S_3 to ($\text{TiO}_2/\text{Ti}_3\text{C}_2\text{T}_x$), the mass ratio of $\text{In}_2\text{S}_3 : \text{TiO}_2 : \text{Ti}_3\text{C}_2\text{T}_x$ should be 1: 0.1 : 0.022.

These microcosmic structures have been confirmed by the transmission electron microscopy (TEM) image of InTi-16 and the high-resolution TEM (HRTEM) image. Compared with the layered $\text{Ti}_3\text{C}_2\text{T}_x$ (Fig. 4a) and the agglomerated In_2S_3 nanoparticles (Fig. 4b), Fig. 4c clearly demonstrates that plentiful nanoparticles filled into the interior of $\text{Ti}_3\text{C}_2\text{T}_x$, or coat onto the edges. The element mapping of InTi-16 by high angle annular dark field scanning transmission electron microscopy (HAADF-STEM) in Fig. 4g indicates the existence and homogeneous distribution of the S, In, Ti, O and C elements. Clearly, the density of S and In elements were greater than that of the Ti, O and C elements, implying that the $\text{TiO}_2/\text{Ti}_3\text{C}_2\text{T}_x$ composite was enclosed by the In_2S_3 nanoparticles to form the quasi-core-shell structure. HRTEM revealed the heterojunction formation of individual stretched In_2S_3 nanoparticles and TiO_2 crystals with well-defined lattice fringes on the $\text{Ti}_3\text{C}_2\text{T}_x$ substrate. Fig. 4d shows that two types of lighter-shade regular stripes corresponding to In_2S_3 crystals and TiO_2 crystals, and irregular-shaped lattice reflecting $\text{Ti}_3\text{C}_2\text{T}_x$. The clear inter-planar distance is measured to be 0.268 nm and 0.238 nm, corresponding to the (400) plane and the (004) plane for cubic In_2S_3 and anatase TiO_2 , respectively. Interestingly, when the TiO_2 combined with the In_2S_3 nanoparticles, the lattice stripes of the In_2S_3 nanoparticles became less distinct. A similar phenomenon has been observed for the lattice stripes of TiO_2 when contacting with $\text{Ti}_3\text{C}_2\text{T}_x$. These results suggest that the In_2S_3 nanoparticles integrated compactly on the surface of TiO_2 , and the TiO_2 grew onto the $\text{Ti}_3\text{C}_2\text{T}_x$ to construct a well-defined dual-heterojunction structure. This also provides proof of the generation of the quasi-core-shell structure of In_2S_3 nanoparticles/ $\text{TiO}_2@/\text{Ti}_3\text{C}_2\text{T}_x$ composite. Two kinds of heterojunctions are mainly included: the $\text{In}_2\text{S}_3/\text{TiO}_2$ type-II heterojunction and $\text{TiO}_2/\text{Ti}_3\text{C}_2\text{T}_x$ Schottky-junction. These well-designed heterojunctions are highly desirable to provide superior charge transfer channels for decreasing the recombination of electro-hole pairs during photochemical reaction.

The Raman spectra of $\text{Ti}_3\text{C}_2\text{T}_x$, $\text{Ti}_3\text{C}_2\text{T}_x\text{-}180$, and InTi-16 have been

recorded with 633 nm excitation sources. As shown in Fig. 5a, the Raman peaks of $\text{Ti}_3\text{C}_2\text{T}_x$ centered at 405 cm^{-1} and 606 cm^{-1} were observed, which can be attributed to the vibrations from non-stoichiometric titanium carbide [59,60]. The two broad peaks between 1348 cm^{-1} and 1581 cm^{-1} are characterized to the D and G modes of graphitic carbon (Fig. 5b). The D-band is associated with the amorphous carbon or deformation vibrations of the hexagonal ring, whereas the G-band to the stacking of the graphite hexagon network plane [61]. After the hydrothermal process with or without In_2S_3 , three other peaks at 392 , 511 and 634 cm^{-1} were indexed to the following anatase vibrational modes of $\text{B}_{1g(1)}$, $\text{A}_{1g}\&\text{B}_{1g(2)}$ and $\text{E}_{g(3)}$, respectively [62]. The ratios of the D- and G-band intensities ($I_{\text{D}}/I_{\text{G}}$) for $\text{Ti}_3\text{C}_2\text{T}_x$, $\text{Ti}_3\text{C}_2\text{T}_x\text{-}180$ and InTi-16 were 0.93, 0.81 and 0.89, respectively, implying the decrease of highly disordered (amorphous) carbon and the outward migration of innermost Ti atoms from the $\text{Ti}_3\text{C}_2\text{T}_x$ structure to react with oxygen [62]. Interestingly, the Raman band centered at 606 cm^{-1} shifts to 634 cm^{-1} after hydrothermal reaction, suggesting the decrease in the inter-space because of the deposition (or growth) of In_2S_3 and TiO_2 particles padding. The appearance of new peak at 509 confirms the formation of anatase TiO_2 phase [63]. Meanwhile, the intensities of D-bands also relatively decrease with no impact on the G-bands, which is the proof of the increase of ordered structure. The existing D and G bands combined with slightly red-shifted Ti-C band clearly indicate that the main Ti_3C_2 sheet structure is still preserved. The SEM, TEM, TGA, XRD and Raman spectra results collectively indicate that, the quasi-core-shell In_2S_3 /anatase $\text{TiO}_2@/\text{metallic Ti}_3\text{C}_2\text{T}_x$ heterostructured hybrids was successfully synthesized with well-defined dual-heterojunction structure.

3.2. Porosity and optical property

The porosity and surface area of materials affects the mass transfer process. N_2 adsorption–desorption isotherms of pure $\text{Ti}_3\text{C}_2\text{T}_x$ and InTi-16 hybrids are shown in Fig. 6, InTi-16 exhibits a type IV isotherm with the H3 hysteresis loop characteristic of mesoporous solids. The surface area of pure In_2S_3 nanoparticles has been reported to be $110\text{ m}^2\text{ g}^{-1}$ with pore volume of $0.38\text{ cm}^3\text{ g}^{-1}$ [54]. The specific surface area and pore volume of InTi-16 were $44.994\text{ m}^2\text{ g}^{-1}$ and $0.163\text{ cm}^3\text{ g}^{-1}$, respectively, which are an order-of-magnitude higher than that of pure $\text{Ti}_3\text{C}_2\text{T}_x$ ($5.154\text{ m}^2\text{ g}^{-1}$ and $0.024\text{ cm}^3\text{ g}^{-1}$, respectively). The increase of the surface area is due to the presence of In_2S_3 or TiO_2 nanoparticles on the edge or surface of $\text{Ti}_3\text{C}_2\text{T}_x$.

Photocatalytic performance is governed by three major processes, namely, light absorption, charge separation and transfer, and surface redox reactions. The light-harvesting capability of the as-obtained photocatalyst was measured by the ultraviolet-visible diffuse reflectance spectra. As displayed in Fig. 7, the $\text{Ti}_3\text{C}_2\text{T}_x$ exhibited no obvious absorption edge in the 310–800 nm region, suggesting the metallic nature of $\text{Ti}_3\text{C}_2\text{T}_x$. After the 180 °C hydrothermal reaction, the absorption edge appears at 400 nm due to the presence of anatase TiO_2 . Compared with the pure In_2S_3 , the light absorption throughout the entire region of 310–800 nm with the absorption edges at 578 nm were similar for InTi-8 and InTi-16. However, with the increment of $\text{Ti}_3\text{C}_2\text{T}_x$, the absorption edge displayed a red-shift to 598 nm and 610 nm, which is due to the synergistic effect between In_2S_3 and TiO_2 (or the OH termination of Ti_3C_2) via significant interfacial coupling interaction and the relatively lower content of In_2S_3 . Among all the InTi-based samples, light absorption in the range of 578 nm–800 nm increased with the increase of $\text{Ti}_3\text{C}_2\text{T}_x$, attributed to the distinctive adsorption of carbonaceous materials [37]. The different optical properties may result in varying photocatalytic performance of the photocatalyst.

3.3. Macroscopic evaluation and analysis of photocatalytic performance

Heterogeneous photocatalysis has been extensively used in the elimination of environmental pollutants. Photocatalytic performance is

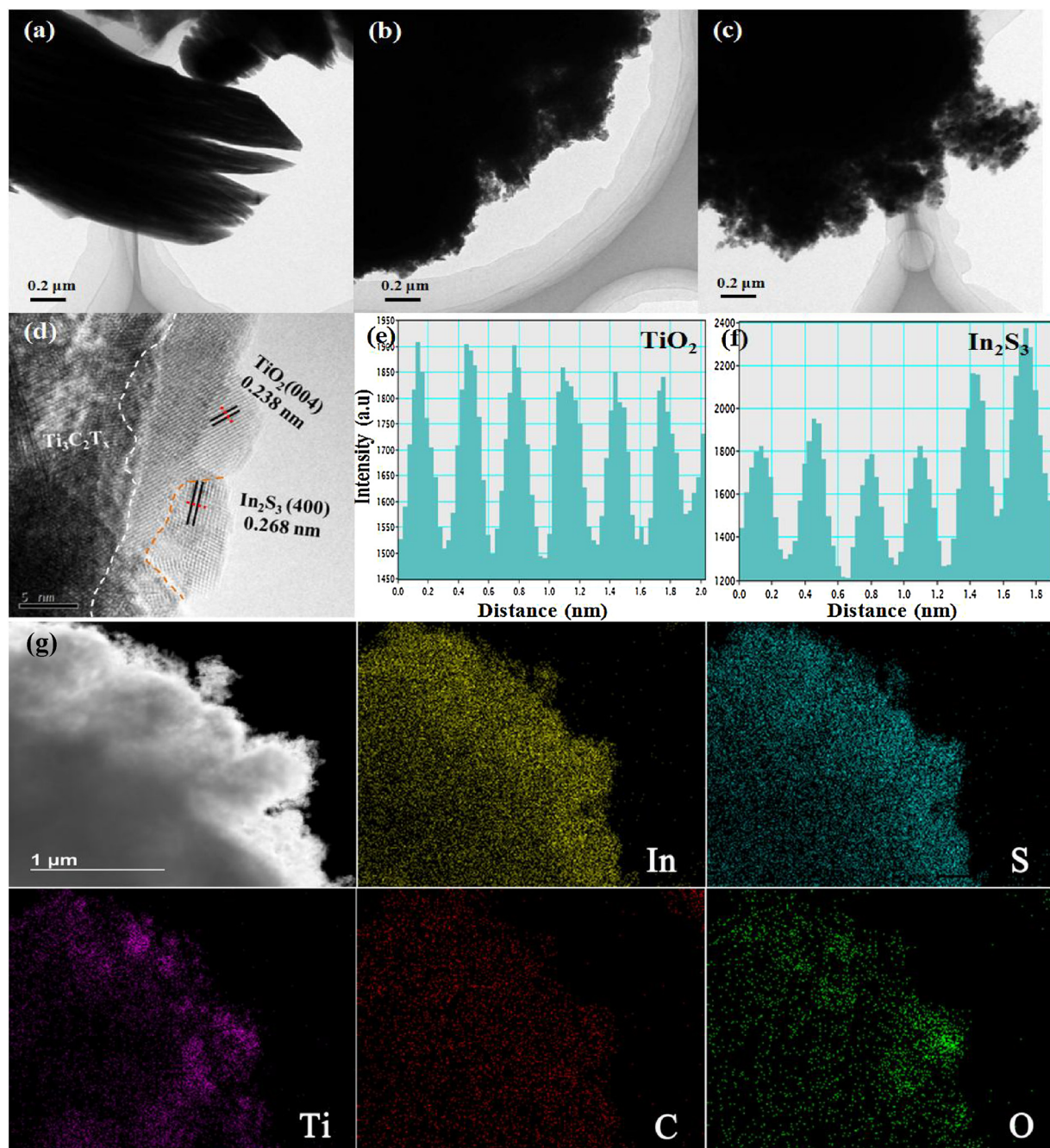


Fig. 4. TEM images of (a) pure $\text{Ti}_3\text{C}_2\text{T}_x$, (b) pure In_2S_3 , and (c, d) InTi-16; (e, f) intensity profiles along the red line in the HRTEM image in (d); and (g) element mapping of InTi-16 by high angle annular dark field scanning transmission electron microscopy (HAADF-STEM) (For interpretation of the references to colour in this figure legend, the reader is referred to the web version of this article).

typically evaluated by liquid-phase degradation of stable pollutant (e.g., MO) solution using the visible light as the solar source under ambient conditions. As shown in Fig. 8a, blank experiments (without catalyst or no light) showed negligible changes for MO concentration, demonstrating the auto-degradation was negligible. Compared with pure In_2S_3 (61.9%) and pure $\text{Ti}_3\text{C}_2\text{T}_x$ (36.0%), all of InTi hybrids exhibited higher photocatalytic MO degradation efficiency within 60 min. The MO photodegradation of $\text{Ti}_3\text{C}_2\text{T}_x$ has been inferentially ascribed to dye photosensitization effect [64,65]. Although the $\text{Ti}_3\text{C}_2\text{T}_x$ had low surface area, the relatively high adsorption capacity was due to the electrostatic attraction between the negatively charge of $\text{Ti}_3\text{C}_2\text{T}_x$ and positively charge MO [27]. The InTi-16 had the highest removal efficiency of 92.1% (Fig. 8a), and a removal efficiency of total organic

carbon of 21.4%, indicating the gradual mineralization of the organic pollutant. From the LC-MS results, different intermediate compounds during the degradation pathway of MO (Fig. S(4,5)) were analyzed. The demethylation of MO or addition of a hydroxyl group to MO led to the formation of intermediates with m/z values of 290.0 and 320.0. On the other hand, the breaking of the azo and ring bonds gave rise to the generation of more small molecules with m/z values of 156.9 and 172.0. These formed intermediates were finally mineralized into CO_2 , H_2O , SO_4^{2-} and NO_3^- [66–69]. However, it was also experimentally demonstrated that the adsorptivity of InTi-16 for MO in the dark was negligible, which is much lower than that for pure In_2S_3 (4.2 mg/g) and pure $\text{Ti}_3\text{C}_2\text{T}_x$ (13.8 mg/g). Herein, dye-photosensitization phenomenon could be excluded for all of InTi hybrids because of the insignificant MO

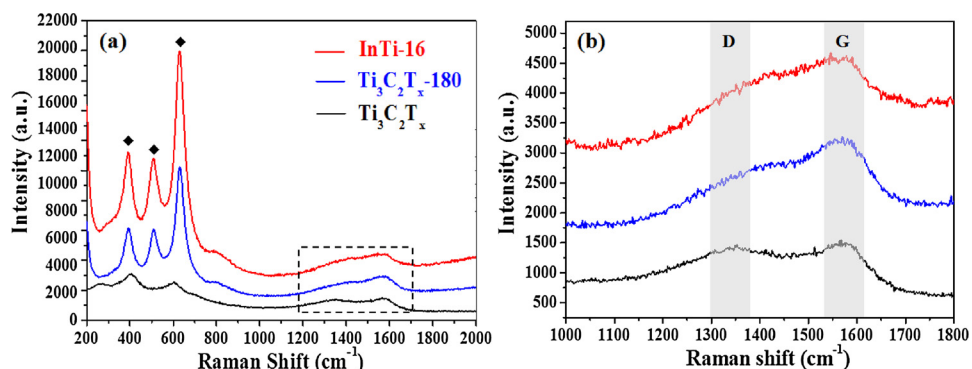


Fig. 5. (a) Raman spectra of pure Ti₃C₂T_x, Ti₃C₂T_x-180 and InTi-16; and (b) magnified Raman spectra from (a) in the Raman shift range of 1000–1800 cm⁻¹.

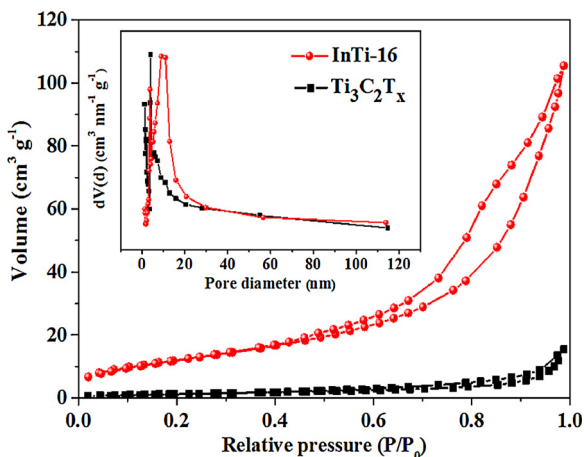


Fig. 6. N₂ adsorption–desorption isotherms of pure Ti₃C₂T_x and InTi-16 hybrids; the inset is the corresponding pore size distribution.

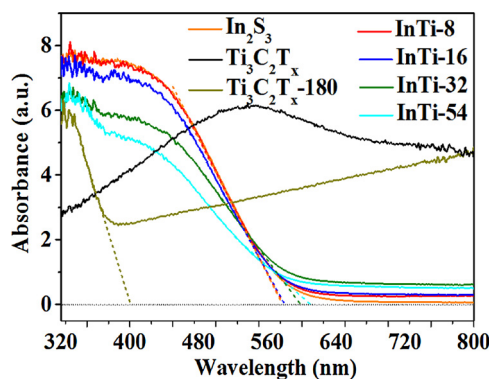


Fig. 7. UV-vis DRS of the photocatalysts.

adsorption. In order to check the photocatalytic degradation performance of InTi-6, the colorless tetracycline hydrochloride (TC) was also tested as a target pollutant. As shown in Fig. S6, the removal efficiency was 62.6% after 120 min with the degradation rate of 0.00745 min⁻¹ under visible light exposure. These also affirm that the significantly enhanced photocatalytic performance of these hybrids did not stem from substrate adsorptivity and dye-photosensitization phenomena.

Photocatalytic degradation rate is a key quantitatively parameter to evaluate the performance of the photocatalyst. The pseudo-first order model ($\ln(C/C_0) = kt$, where k is the rate constant) was applied to model kinetic behavior. As shown in Fig. 8b, the MO degradation rate is the fastest for InTi-16 (0.04977 min⁻¹), followed by InTi-8 (0.04344 min⁻¹), InTi-32 (0.03192 min⁻¹), InTi-54 (0.03103 min⁻¹), physical mixture (0.01844 min⁻¹), In₂S₃ (0.01536 min⁻¹), and lastly

Ti₃C₂T_x (0.00799 min⁻¹). The visible-light photocatalytic performance of InTi-16 is 3.2 and 6.2 folds higher than that of pure In₂S₃ and pure Ti₃C₂T_x, respectively. As the Ti₃C₂T_x content increased in the hybrid photocatalysts, the photocatalytic performance increased and then decreased. This trend is contradictory to the results of the UV-vis DRS (Fig. 7), indicating that the enhanced visible-light absorption was unlikely to promote the enhancement of photocatalytic performance observed for InTi hybrids. Therefore, it can be alternatively inferred that the synergistic effect between In₂S₃ and Ti₃C₂T_x effectively enhances the photocatalytic degradation ability of hybrids, which is mainly through photoinduced interfacial charge transfer at the hybridized heterojunction and prolong the electron lifetime. With the increment of Ti₃C₂T_x, more In³⁺ are adsorbed onto the adsorption sites of Ti₃C₂T_x, creating more heterojunction sites for charge transfer. However, excessive Ti₃C₂T_x generates more anatase TiO₂, which adversely affected the charge transfer since the conductivity of TiO₂ is far lower than that of Ti₃C₂T_x. Moreover, the TiO₂ decreases the quality of effective heterojunction interfaces or serves as the recombination centre for hindering the charge transfer. To study the importance of the chemical interactions formed between In₂S₃, TiO₂ and Ti₃C₂T_x for MO degradation, the sample with the same weight ratio as InTi-16 was prepared via physical mixing. The photocatalytic performance of the physically mixed sample was much lower than that of other InTi-based materials, indicating the interfacial interaction among the three components in the hybrids was key to enhancing the photocatalytic reaction [65]. Throughout eight repeated degradation-regeneration cycles, the MO removal efficiency was sustained above 90% (Fig. 8e), indicating the In₂S₃/TiO₂@Ti₃C₂T_x heterostructured hybrid exhibited excellent reusability. After the photocatalytic process, the InTi-16 was rinsed by deionized water two times and dried in air or vacuum. Then the crystal data was measured via XRD diffractometer. Fig. 8f shows that the crystal structure of InTi-16 after different durations of MO photodegradation and with drying under vacuum was consistent with that before photocatalysis. Furthermore, the In ions in solution after visible light irradiation was detected by inductively coupled plasma mass spectrometry (ICP-MS). The total indium content initially added in solution was 352 mg/L, and decreased to 0.156 mg/L after the photocatalytic process. So the In₂S₃/TiO₂@Ti₃C₂T_x heterostructured hybrids still had good stability. Interestingly, if the used photocatalyst was dried in air, some new peaks at 19.2°, 22.7° and 38.1° appeared and the peak intensity at 25.6° increased when compared with the fresh photocatalyst. These new peaks correspond to the Ti₆O₁₁ (TiO_{1.83}, PDF#50-0788) of TiO_{2-x} Magneli phase with oxygen deficiency [70,71]. The existence of oxygen vacancies also facilitated the photocatalytic degradation performance [72].

To examine the advantages of the In₂S₃/TiO₂@Ti₃C₂T_x for photocatalytic application, we prepared a few more In₂S₃-based systems including In₂S₃/CNT, In₂S₃/rGO, In₂S₃/MoS₂, and In₂S₃/TiO₂ using the same synthesis protocol. In Fig. S7 and S8, the crystallinity and morphology of these hybrids are indicative of successful preparation. A

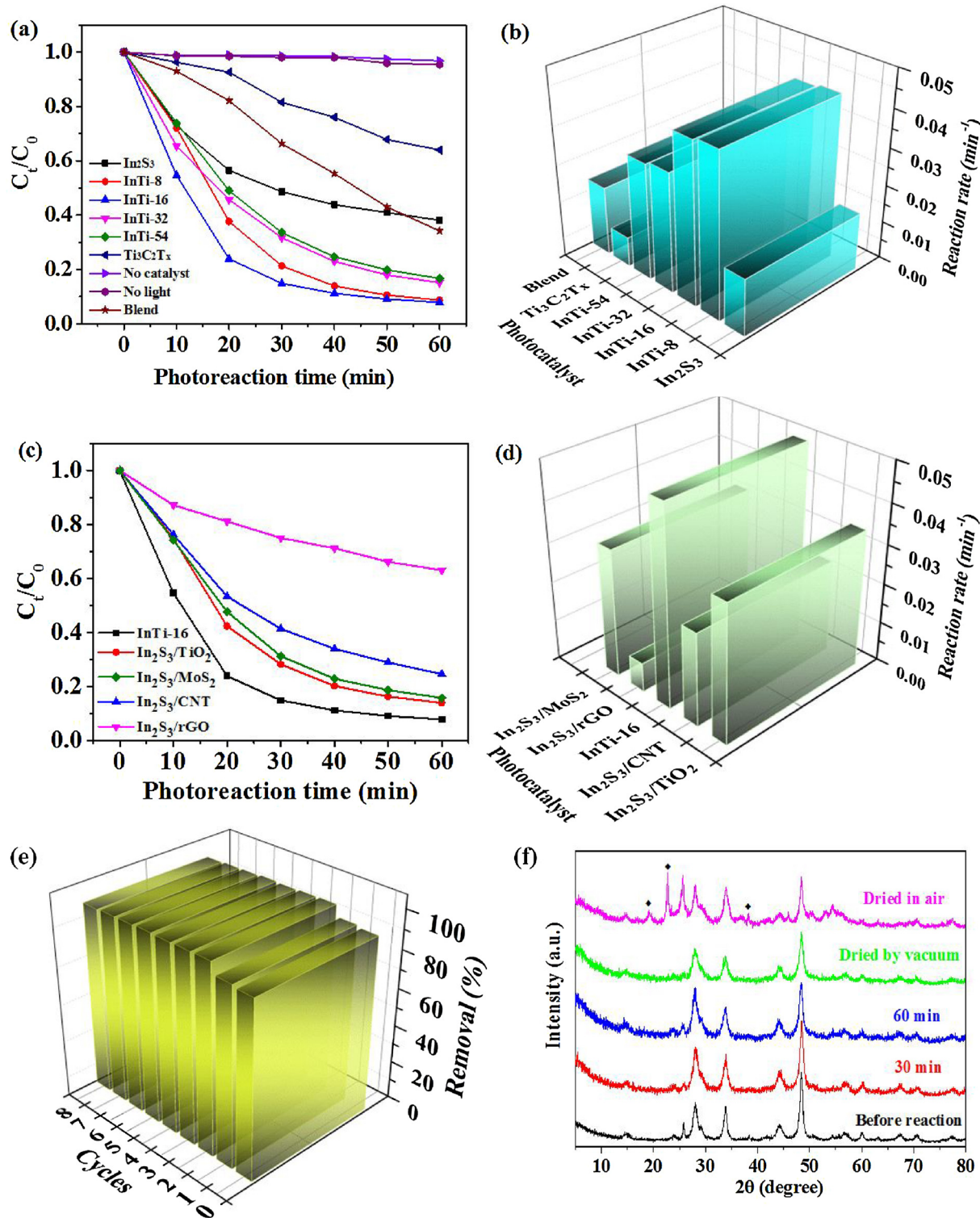


Fig. 8. (a,c) Photocatalytic degradation of MO with time and (b,d) pseudo-first order rate constants for pure In_2S_3 , pure $\text{Ti}_3\text{C}_2\text{T}_x$, InTi hybrids (“blend” represents the physically mixed sample of In_2S_3 , TiO_2 and $\text{Ti}_3\text{C}_2\text{T}_x$ with the mass ratio of 1 : 0.1 : 0.022) and In_2S_3 -based hybrids; and (e,f) recyclability and stability tests of InTi-16 for the photodegradation of MO under visible light irradiation.

comparison of the photocatalytic degradation ability of InTi-16 with respect to the $\text{In}_2\text{S}_3/\text{CNT}$, $\text{In}_2\text{S}_3/\text{rGO}$, $\text{In}_2\text{S}_3/\text{MoS}_2$, and $\text{In}_2\text{S}_3/\text{TiO}_2$ hybrids are shown in Fig. 8c and d. Clearly, InTi-16 had the highest degradation efficiency and photocatalytic degradation rate for MO removal compared to all of In_2S_3 -based hybrids. The photocatalytic degradation performance of InTi-16 was 1.4, 2.1, 6.8 and 1.5 times higher than that of $\text{In}_2\text{S}_3/\text{TiO}_2$, $\text{In}_2\text{S}_3/\text{CNT}$, $\text{In}_2\text{S}_3/\text{rGO}$ and $\text{In}_2\text{S}_3/\text{MoS}_2$,

respectively. This indicates the quasi-core-shell $\text{In}_2\text{S}_3/\text{anatase TiO}_2@$ metallic $\text{Ti}_3\text{C}_2\text{T}_x$ heterostructured hybrid exhibited superior photocatalytic capability for pollutant degradation. The different photocatalytic performances could be based on the following plausible hypothesis. The $\text{Ti}_3\text{C}_2\text{T}_x$ ($T = \text{OH}$) has ultralow work function (1.6–2.8 eV), which is much lower than that of rGO (4.89–5.16 eV), CNT (5.05 eV), MoS_2 (4.04 eV) and TiO_2 (4.92 eV) [73–77]. In parallel,

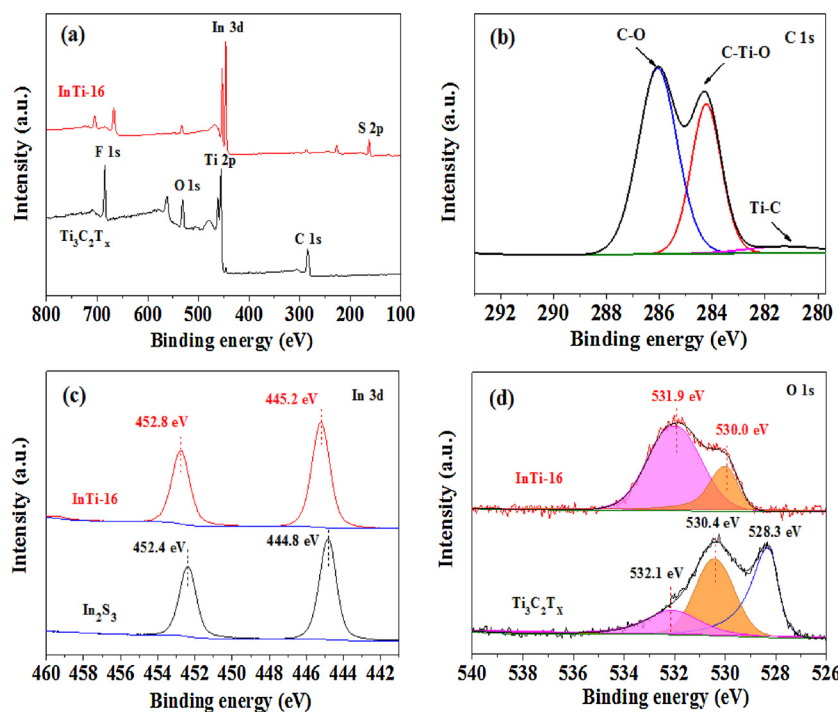


Fig. 9. XPS spectra of InTi-16: (a) survey scan, (b) C 1 s, (c) In 3d, and (d) O 1 s. For comparison, the survey scan of $\text{Ti}_3\text{C}_2\text{T}_x$, the In 3d spectra of In_2S_3 and the O 1 s spectra of $\text{Ti}_3\text{C}_2\text{T}_x$ are also shown.

although $\text{Ti}_3\text{C}_2\text{T}_x$ has a large amount of termination groups ($-\text{O}$, $-\text{OH}$ and $-\text{COO}$), the constructed synergistic double-heterojunctions and $\text{Ti}_3\text{C}_2\text{T}_x$ with significant anisotropic carrier (electron and hole) mobility and good electrical conductivity facilitates the separation of photo-generated electron–hole pairs [30,33]. On the other hand, graphene and carbon nanotube usually suffer markedly conductivity loss after groups decoration [78]. Last but not the least, the synergistic action of many factors, including the precursors and corresponding amount, particle size, specific surface area, composition and dispersibility, etc, may also result in the difference in photocatalytic performance of In_2S_3 -based samples. All in all, it can be concluded that the $\text{Ti}_3\text{C}_2\text{T}_x$ and partly derived TiO_2 can serve as an advantageous platform for the in situ immobilization of In_2S_3 nanoparticles for photocatalytic application.

3.4. Charge separation and transfer via heterojunction interfaces

Heterojunction provides a special channel for photoinduced charge mobility in hybrids, which also were characterized via the surface chemical state and the coupling interaction between each component. From the XPS spectra in Fig. 9a, the peaks of F element in the survey spectrum of InTi-16 disappeared, indicating the F element has been exchanged during the hydrothermal reaction. In the case of the C 1 s pattern of InTi-6 (Fig. 9b), three peaks at 286.1, 284.2 and 281.3 eV can be deconvoluted, which are ascribed to C–O, C–Ti–O and Ti–C bonds, respectively [39]. This provides the other proof that the main $\text{Ti}_3\text{C}_2\text{T}_x$ structure was still retained. From Fig. 9c, the binding energies of In 3d in In_2S_3 at 452.4 eV and 444.8 eV correspond to $\text{In} 3d_{3/2}$ and $\text{In} 3d_{5/2}$, respectively, validating the existence of In(III) [45]. However, the binding energies of $\text{In} 3d_{3/2}$ and $\text{In} 3d_{5/2}$ shifted to 452.8 eV and 445.2 eV, respectively, after the addition of $\text{Ti}_3\text{C}_2\text{T}_x$. The binding energy shifts imply that there were additional coulombic interaction between the emitted electron and the indium core. Furthermore, with respect to the O 1 s XPS spectra of $\text{Ti}_3\text{C}_2\text{T}_x$ (Fig. 9d), three peaks at 528.3, 530.4 and 532.1 eV were deconvoluted, corresponding to respectively the surface adsorbed O species, the Ti–O–Ti and the Ti–OH onto the surface termination of Ti_3C_2 , respectively [37]. After the immobilization of In_2S_3 , the binding energy shifts to 530.0 eV and

531.9 eV, which denotes lower binding energy compared to that in pure $\text{Ti}_3\text{C}_2\text{T}_x$. This suggests that, the *p*-orbital of O atoms can interact with the unoccupied *d*-orbitals of In atoms to form In–O bond with the minimal space constraint. Such chemical coupling led to increased electron density in O atoms along with decreased electron density in In atoms to form covalent $\text{In}(\delta^+)-\text{O}(\delta^-)$ bonding state. The strong interfacial coupling interaction between In_2S_3 and TiO_2 became favorable charge transfer ways. In Fig. S9, compared with $\text{Ti}_3\text{C}_2\text{T}_x$, a negative shift of Ti 2p for the binding energy of InTi-16 is shown, implying that the charge was changed dramatically to less positive. As the hybridization increased between O and Ti due to the larger overlap between the O 2p and Ti 3d orbitals, the O 2p band centre shifted, resulting in the increase of the work functions in the OH terminated $\text{Ti}_3\text{C}_2\text{T}_x$ [79]. The remaining positive charges in TiO_2 near the $\text{TiO}_2/\text{Ti}_3\text{C}_2\text{T}_x$ interface facilitated the formation of the space charge layer, inducing the upward band bending of the conductor band (CB) and valence band (VB) of TiO_2 [80]. With the gradual accumulation of electron, the Fermi level of $\text{Ti}_3\text{C}_2\text{T}_x$ would rise and subsequently attain the equilibrium of $\text{Ti}_3\text{C}_2\text{T}_x$ in the InTi-16 system. Finally, a Schottky junction was formed between TiO_2 and $\text{Ti}_3\text{C}_2\text{T}_x$. A similar phenomenon had been demonstrated by Ran et al. [24] and Jakob et al. [81]. Therefore, the well-defined heterojunctions provide favorable channels for rapid charge transfer in the photochemical reaction process.

To shed light on the influence of heterojunctions with a host of charge transfer channels on the photoinduced exciton separation and carrier transfer efficiency, the steady-state and time-resolved PL spectra, TPC response and EIS were measured. As shown in Fig. 10a, the quenched emission peak of InTi-16 under the excitation wavelength of 330 nm was lower than that of pure In_2S_3 due to the preferential segregation of energetic electrons onto TiO_2 and $\text{Ti}_3\text{C}_2\text{T}_x$, suggesting the recombination of photo-excited charge carriers was efficiently suppressed in the presence of TiO_2 and $\text{Ti}_3\text{C}_2\text{T}_x$. The time-resolved PL spectra show that the charge carrier lifetime elongated from 0.42 ns for In_2S_3 to 0.84 ns for InTi-16 (Figs. 10b and S11). The bulk charge-transfer efficiency investigated by TPC response (Fig. 10c) shows that the photocurrent density of InTi-16 was $9.60 \mu\text{A cm}^{-2}$, which is higher than that of pure In_2S_3 ($2.66 \mu\text{A cm}^{-2}$). The observed improvement on

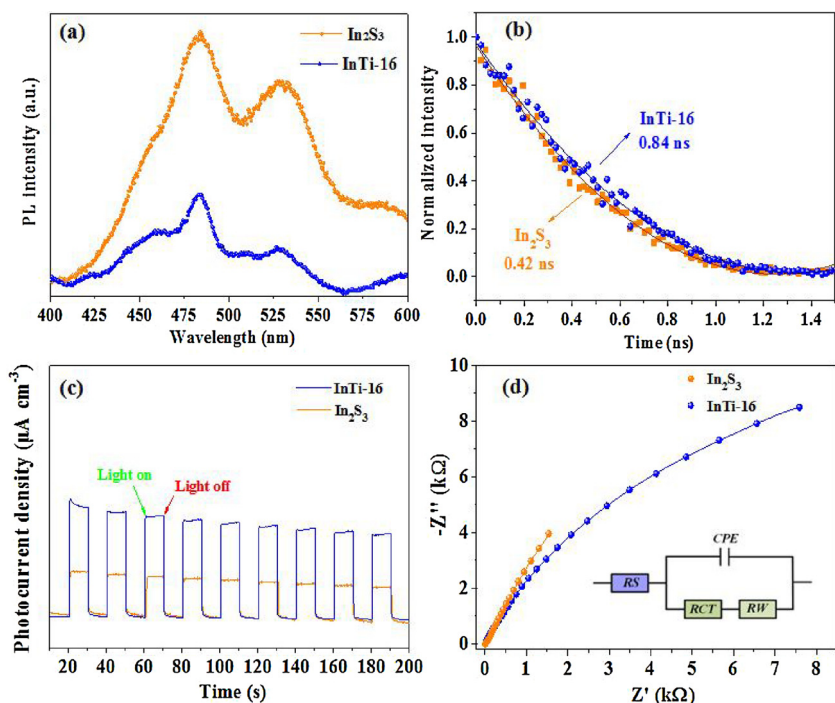


Fig. 10. Steady-state PL spectra (a) and time-resolved PL spectra (b) of In₂S₃ and InTi-16. Transient photocurrent responses (c) and electrochemical impedance spectroscopy (EIS) changes (d) of In₂S₃ and InTi-16.

loading of the TiO₂ and Ti₃C₂T_x directly reflects the enhanced efficiency of photogenerated exciton separation and carrier transport in bulk InTi-16. From the EIS Nyquist analysis (Fig. 10e), InTi-16 exhibited a much smaller semicircle diameter than of pure In₂S₃ under visible-light irradiation in 0.5 M Na₂SO₄ electrolyte solution, suggesting a much lower interfacial charge-transfer resistance and an apparent augmentation of interfacial charge-carrier transfer on the surface of InTi-16. From the above analysis, it can be concluded that the origin of excellent photocatalytic degradation ability for InTi-16 is due to the photoinduced exciton separation and carrier transfer via a multitude of charge transfer channels due to the formation of double heterojunctions structure (type-II heterojunction and Schottky junction) among In₂S₃, TiO₂ and Ti₃C₂T_x.

3.5. Mechanism of photocatalytic reaction

After the photogenerated carrier (electron or hole) transfer, the following step in photocatalytic pollutant degradation is the surface redox reaction catalyzed by the reactive sites on InTi-16. It is generally acknowledged that a large amount of oxidative species will form after the redox reaction between the separated free electron or hole in reactive sites and the medium like H₂O, O₂ and even organic species [7,82]. The ESR spin-trap experiments performed using the InTi-16 hybrid as the photocatalyst under visible light irradiation. As shown in Fig. 11a, the intensity of the DMPO-·O₂⁻ in methanol dispersion is negligible in the dark, but becomes greater with longer durations of visible light irradiation, demonstrating that photoinduced generation of the ·O₂⁻ in the photocatalytic process. The ·O₂⁻ is derived from the reduction between photogenerated electron and O₂ since the potentials of the accumulated electrons is more negative than that of the O₂ reduction to ·O₂⁻ ($E_{O_2/O_2^-} = -0.046$ eV) [83]. After the addition of DMPO-·OH adducts, four characteristic peaks (Fig. 11b) appeared, indicating that the ·OH was also produced, which is presumably the reductive pathway. Specifically, the O₂ captured the photogenerated electron to generate ·O₂⁻ and subsequently generated the ·OH. The VB potential of In₂S₃ was more negative than $E_{(·OH/OH^-)}$ (2.38 V vs. NHE) and $E_{(·OH/H_2O)}$ (2.27 V vs. NHE), and thus the way to produce ·

OH via the oxidation of H₂O is thermodynamically impossible. The table 2,2,6,6-tetramethyl-1-piperidinyloxy (TEMPO) free radical can be oxidized by holes. Thus, the disappearance of TEMPO radical ESR spectra (Fig. 11c) upon irradiation confirms the photogenerated holes [84].

Furthermore, in order to verify the contribution of these reactive oxygen species in the photocatalytic degradation of pollutants, different trapping experiments have been carried out using K₂Cr₂O₇ (e⁻ scavenger), ethylenediaminetetraacetic acid disodium salt (EDTA-2Na, h⁺ scavenger), p-benzoquinone (BQ, ·O₂⁻ scavenger), isopropyl alcohol (IPA, ·OH scavengers) or Ar flow (excluding O₂). As shown in Fig. 11d, the photocatalytic degradation of MO was apparently restrained after the injection of K₂Cr₂O₇ and p-benzoquinone. The results indicate that MO degradation mainly depended on the strong oxidative ·O₂⁻, which originated from the O₂ reduction with the aid of photogenerated electron. The relatively weak inhibiting effect after the Ar gas injection indicates that the O₂ was not only from the dissolved O₂ in water, but the water molecules oxidation ($4h^+ + 2H_2O \rightarrow O_{2(VB)} + 4H^+$), because the VB potential of In₂S₃ was more positive than the oxidation potential of water (1.23 V vs. NHE) [83]. The O₂ generation amount of In₂S₃ is displayed in Fig. S12 and the results show that the formed O₂ amount increased with irradiation time. The weak suppression effect for IPA is possibly related to the formed path of ·OH. Meanwhile, the h⁺ was not deemed to participate in the MO degradation directly due to the weakly suppression effect of EDTA-2Na. To sum up, the organic pollutant degradation was principally dependent on the oxidative species of ·O₂⁻ or ·OH or both.

On the basis of the above experimental results, a photocatalytic mechanism illustrating the excellent photocatalytic pollutant degradation of InTi-16 is proposed in Fig. 12. As calculated in Fig. S10, the potentials of conductor band (CB) and valence band (VB) for In₂S₃ are -0.97 eV and 1.37 eV, respectively. Under visible light exposure, the electrons are excited from the VB to the CB of In₂S₃ (Fig. 12a), accompanied by the migration from the CB of In₂S₃ to the CB of TiO₂ via the heterojunction (the covalent In(δ^+)-O(δ^-) bonding state) because of the more negative potential (-0.45 V versus SHE) [85]. For the Ti₃AlC₂ phases, the valence states below the Fermi level were divided

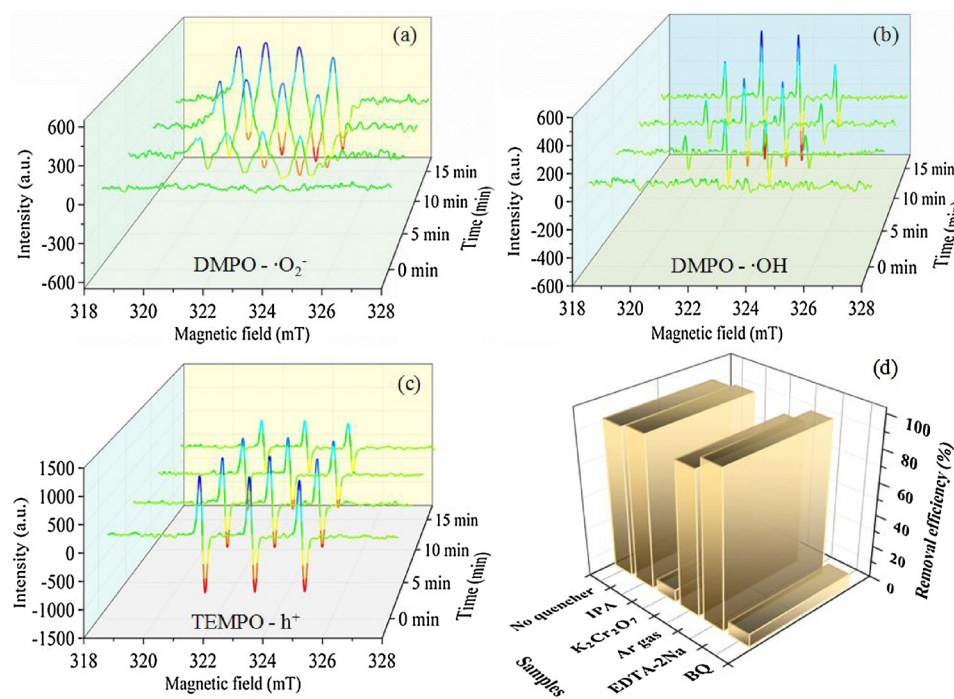


Fig. 11. ESR spectra of radical adducts trapped by DMPO ($\cdot\text{O}_2^-$ and $\cdot\text{OH}$) and TEMPO (h^+) in dispersions under visible light irradiation: (a) in methanol dispersion for DMPO- $\cdot\text{O}_2^-$, (b) in aqueous dispersion for DMPO- $\cdot\text{OH}$ and (c) in aqueous dispersion for TEMPO- h^+ , (d) Effects of different reactive species scavengers on the photodegradation of MO by InTi-16 under visible-light irradiation.

into two sub-bands, namely, the hybridized Ti 3d-C 2p and Ti 3d-Al 3s orbitals (Band B), and the Ti 3d-Al 3p orbitals near the Fermi level (Band A) [86]. After etching to $\text{Ti}_3\text{C}_2\text{T}_x$, Band B was governed by mixed Ti 3d and C 2p bands, and connected with Band A. So the weaker Ti-O coupling in energy states B resulted in the metallic phase of $\text{Ti}_3\text{C}_2\text{O}_2$ [86]. The density of free carriers for $\text{Ti}_3\text{C}_2\text{T}_x$ monolayers has been reported to be $8 \pm 3 \times 10^{21} \text{ cm}^{-3}$, and the electrical conductivity of $\text{Ti}_3\text{C}_2\text{T}_x$ to be $4600 \pm 1100 \text{ S cm}^{-1}$ with the field-effect electron mobility of $2.6 \pm 0.7 \text{ cm}^{-2}\text{V}^{-1}\text{s}^{-1}$ [27]. Owing to the accumulation of negative charge in TiO_2 , the photogenerated electrons across the ‘upward’ bent CB at the $\text{TiO}_2/\text{Ti}_3\text{C}_2\text{T}_x$ interface can be channeled to $\text{Ti}_3\text{C}_2\text{T}_x$ due to the various work function of $\text{Ti}_3\text{C}_2\text{T}_x$ (1.6–2.8 eV) and TiO_2 (4.92 eV). Furthermore, the charge migration caused by the different Fermi levels of TiO_2 and $\text{Ti}_3\text{C}_2\text{T}_x$ led to the formation of a depletion layer at the semiconductor/metal interface. This depletion layer created an energy barrier to prevent the electrons from diffusing back to the TiO_2 species, which also is known as the Schottky junction. The special heterojunction is not the same as Ohmic contacts with the easy

charge flow in both directions between the semiconductor and metal interface. Similar results have been shown in earlier reports [24,37,38,87]. Formed Schottky barrier suppresses the back-diffusion of electrons to the TiO_2 species. The acquired and photo-induced electrons rapidly shuttled to $\text{Ti}_3\text{C}_2\text{T}_x$ surface because of the excellent metallic conductivity, and finally captured by the oxygen molecule to form $\cdot\text{O}_2^-$ at the in-plane of $\text{Ti}_3\text{C}_2\text{T}_x$. Because the in-plane electrical conductivity of $\text{Ti}_3\text{C}_2\text{T}_x$ is at least one order of magnitude higher than that vertical to the basal plane [88]. Meanwhile, the $\cdot\text{O}_2^-$ can further be reduced to produce $\cdot\text{OH}$. The resident hole in In_2S_3 will oxidize H_2O into O_2 , not the $\cdot\text{OH}$ since the potential of VB is more positive than that of $E_{\text{OH}^-/\text{OH}}$. These strong oxidized radical ultimately degrade organic pollutant into CO_2 , H_2O or others (Fig. 12b). It should be emphasized that these charge transfer channels endowed by the two kinds of well-defined heterojunctions greatly enhance the charge transport and separation efficiency and prolong the active electron lifetime, facilitating a remarkable oxidized radical species generation.

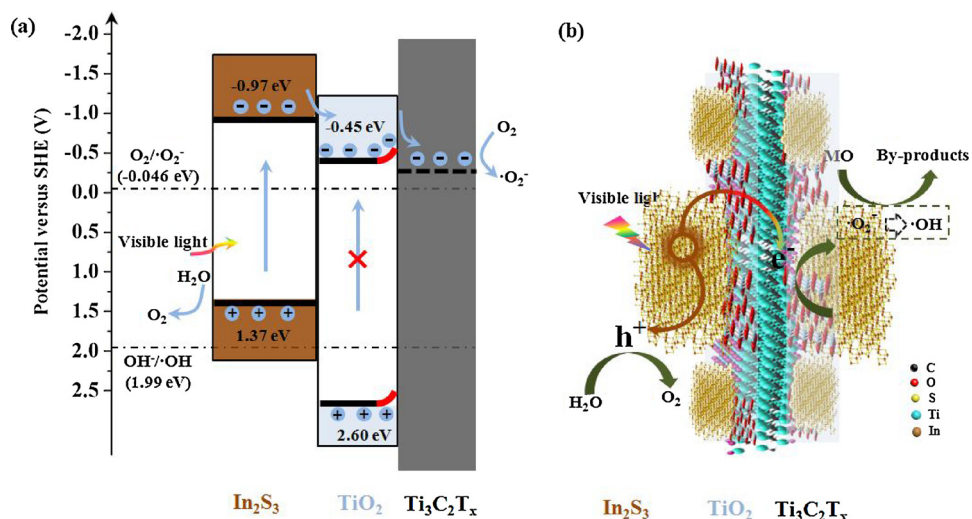


Fig. 12. (a) Charge separation and transfer; and (b) proposed mechanism for pollutant degradation in the InTi-16 system under visible light illumination.

4. Conclusion

New quasi-core-shell structured In_2S_3 /anatase TiO_2 @metallic $\text{Ti}_3\text{C}_2\text{T}_x$ MXene hybrids had been constructed via the *in situ* growth consisting of well-designed type-II heterojunction and non-noble metal-based Schottky junction with favorable charge transfer channels for efficient photocatalysis. This kind of mesoporous hybrids had superior visible-light absorption property and excellent photogenerated-carrier separation capability. Specifically, the hybrid photocatalyst with the additive $\text{Ti}_3\text{C}_2\text{T}_x$ content of 16 mg showed improved visible-light photocatalytic degradation ability towards pollutant removal in water with a degradation rate of 0.04977 min^{-1} , which was 3.2 and 6.2 folds higher than that of pure In_2S_3 and pure $\text{Ti}_3\text{C}_2\text{T}_x$, respectively. In addition, the In-Ti-16 hybrid had the highest degradation efficiency and photocatalytic rate for pollutant removal compared to the $\text{In}_2\text{S}_3/\text{MoS}_2$ and $\text{In}_2\text{S}_3/\text{TiO}_2$ hybrids. The outstanding photocatalytic performance was attributed to the synergistic effect of In_2S_3 visible-light absorption, the band of TiO_2 and the favorable electrical conductivity of $\text{Ti}_3\text{C}_2\text{T}_x$. It endowed the excellent separation and transfer efficiency of photo-generated exciton and carrier via the double heterojunction structure with the aid of charge transfer channels. The prolonger electron lifetime favored for the strongly oxidizing radical generation ($\cdot\text{O}_2^-$) at the in-plane of $\text{Ti}_3\text{C}_2\text{T}_x$ and thus enhanced photocatalytic degradation performance. This study affirms that the metallic $\text{Ti}_3\text{C}_2\text{T}_x$ and derived TiO_2 , seving as new platform, is promising for photocatalytic applications. In view of the results here that demonstrate that the performance of MXene can be tuned by doping, morphology or composition modifications, more MXene-based photocatalytic studies are warranted for advanced catalysis and energy areas.

Acknowledgments

The authors gratefully acknowledge the financial support provided by the Singapore Ministry of Education Academic Research Funds Tier 2 (MOE2014-T2-2-074; ARC16/15) and Tier 1 (2015-T1-001-023; RG7/15), the GSK (GlaxoSmithKline) – EDB (Economic Development Board) Trust Fund, and the Joint Singapore-Germany Research Project Fund (SGP-PROG3-019). We also acknowledge funding from the Foundation for Innovative Research Groups of the National Natural Science Foundation of China (No. 51521006), the Key Project of National Nature Science Foundation of China (No. 51739004), and the Projects of the National Nature Science Foundation of China (No. 21776066, 51708195).

Appendix A. Supplementary data

Supplementary material related to this article can be found, in the online version, at doi:<https://doi.org/10.1016/j.apcatb.2018.04.012>.

References

- [1] J. Liu, Y. Liu, N. Liu, Y. Han, X. Zhang, H. Huang, Y. Lifshitz, S.-T. Lee, J. Zhong, Z. Kang, *Science* 347 (2015) 970–974.
- [2] H. Wang, X. Yuan, Y. Wu, H. Huang, X. Peng, G. Zeng, H. Zhong, J. Liang, M. Ren, *Adv. Colloid Interface Sci.* 195–196 (2013) 19–40.
- [3] M.H. Sun, S.Z. Huang, L.H. Chen, Y. Li, X.Y. Yang, Z.Y. Yuan, B.L. Su, *Chem. Soc. Rev.* 45 (2016) 3479–3563.
- [4] H. Wang, X. Yuan, G. Zeng, Y. Wu, Y. Liu, Q. Jiang, S. Gu, *Adv. Colloid Interface Sci.* 221 (2015) 41–59.
- [5] K.S. Novoselov, A. Mishchenko, A. Carvalho, A.H. Castro Neto, *Science* 353 (2016) aac9439.
- [6] F. Bonaccorso, L. Colombo, G.H. Yu, M. Stoller, V. Tozzini, A.C. Ferrari, R.S. Ruoff, V. Pellegrini, *Science* 347 (2015) 1246501.
- [7] L. Jiang, X. Yuan, Y. Pan, J. Liang, G. Zeng, Z. Wu, H. Wang, *Appl. Catal. B Environ.* 217 (2017) 388–406.
- [8] L. Jiang, X. Yuan, G. Zeng, X. Chen, Z. Wu, J. Liang, J. Zhang, H. Wang, H. Wang, *ACS Sustain. Chem. Eng.* 5 (2017) 5831–5841.
- [9] W. Lei, G. Liu, J. Zhang, M. Liu, *Chem. Soc. Rev.* 46 (2017) 3492–3509.
- [10] D. Deng, K.S. Novoselov, Q. Fu, N. Zheng, Z. Tian, X. Bao, *Nat. Nano* 11 (2016) 218–230.
- [11] Q. Weng, X. Wang, X. Wang, Y. Bando, D. Golberg, *Chem. Soc. Rev.* 45 (2016) 3989–4012.
- [12] Z. Yang, F. Wang, C. Zhang, G. Zeng, X. Tan, Z. Yu, Y. Zhong, H. Wang, F. Cui, *RSC Adv.* 6 (2016) 79415–79436.
- [13] Q.P. Lu, Y.F. Yu, Q.L. Ma, B. Chen, H. Zhang, *Adv. Mater.* 28 (2016) 1917–1933.
- [14] H. Wang, X. Yuan, Y. Wu, X. Chen, L. Leng, G. Zeng, *RSC Adv.* 5 (2015) 32531–32535.
- [15] Y.J. Ding, Y.P. Chen, X.L. Zhang, L. Chen, Z.H. Dong, H.L. Jiang, H.X. Xu, H.C. Zhou, *J. Am. Chem. Soc.* 139 (2017) 9136–9139.
- [16] J. Thote, H.B. Aiyappa, A. Deshpande, D.D. Diaz, S. Kurungot, R. Banerjee, *Chem. Eur. J.* 20 (2014) 15961–15965.
- [17] M. Ghidiu, M.R. Lukatskaya, M.Q. Zhao, Y. Gogotsi, M.W. Barsoum, *Nature* 516 (2014) 78–81.
- [18] F. Shahzad, M. Alhabeb, C.B. Hatter, B. Anasori, S.M. Hong, C.M. Koo, Y. Gogotsi, *Science* 353 (2016) 1137–1140.
- [19] M.R. Lukatskaya, O. Mashtalir, C.E. Ren, Y. Dall'Agnese, P. Rozier, P.L. Taberna, M. Naguib, P. Simon, M.W. Barsoum, Y. Gogotsi, *Science* 341 (2013) 1502–1505.
- [20] B. Anasori, M.R. Lukatskaya, Y. Gogotsi, *Nat. Rev. Mater.* 2 (2017) 16098.
- [21] M. Naguib, V.N. Mochalin, M.W. Barsoum, Y. Gogotsi, *Adv. Mater.* 26 (2014) 992–1005.
- [22] V.M. Hong Ng, H. Huang, K. Zhou, P.S. Lee, W. Que, J.Z. Xu, L.B. Kong, *J. Mater. Chem. A* 5 (2017) 3039–3068.
- [23] C. Xu, L. Wang, Z. Liu, L. Chen, J. Guo, N. Kang, X.L. Ma, H.M. Cheng, W. Ren, *Nat. Mater.* 14 (2015) 1135–1141.
- [24] J. Ran, G. Gao, F.T. Li, T.Y. Ma, A. Du, S.Z. Qiao, *Nat. Commun.* 8 (2017) 13907.
- [25] Q. Peng, J. Guo, Q. Zhang, J. Xiang, B. Liu, A. Zhou, R. Liu, Y. Tian, *J. Am. Chem. Soc.* 136 (2014) 4113–4116.
- [26] Z. Ling, C.E. Ren, M.Q. Zhao, J. Yang, J.M. Giamarco, J.S. Qiu, M.W. Barsoum, Y. Gogotsi, *Proc. Natl. Acad. Sci. U. S. A.* 111 (2014) 16676–16681.
- [27] L. Ding, Y. Wei, Y. Wang, H. Chen, J. Caro, H. Wang, *Angew. Chem. Int. Ed.* 56 (2017) 1825–1829.
- [28] Q. Xue, H. Zhang, M. Zhu, Z. Pei, H. Li, Z. Wang, Y. Huang, Y. Huang, Q. Deng, J. Zhou, S. Du, Q. Huang, C. Zhi, *Adv. Mater.* 29 (2017) 1604847.
- [29] H. Wang, Y. Wu, X. Yuan, G. Zeng, J. Zhou, X. Wang, J.W. Chew, *Adv. Mater.* 30 (2017), <http://dx.doi.org/10.1002/adma.201704561> 1704561.
- [30] M. Khazaei, A. Ranjbar, M. Arai, T. Sasaki, S. Yunoki, *J. Mater. Chem. C* 5 (2017) 2488–2503.
- [31] H. Zhang, G. Yang, X. Zuo, H. Tang, Q. Yang, G. Li, *J. Mater. Chem. A* 4 (2016) 12913–12920.
- [32] Z. Guo, J. Zhou, L. Zhu, Z. Sun, *J. Mater. Chem. A* 4 (2016) 11446–11452.
- [33] L. Zhao, B. Dong, S. Li, L. Zhou, L. Lai, Z. Wang, S. Zhao, M. Han, K. Gao, M. Lu, X. Xie, B. Chen, Z. Liu, X. Wang, H. Zhang, H. Li, J. Liu, H. Zhang, X. Huang, W. Huang, *ACS Nano* 11 (2017) 5800–5807.
- [34] X. Sang, Y. Xie, M.W. Lin, M. Alhabeb, K.L. Van Aken, Y. Gogotsi, P.R. Kent, K. Xiao, R.R. Unocic, *ACS Nano* 10 (2016) 9193–9200.
- [35] O. Mashtalir, K.M. Cook, V.N. Mochalin, M. Crowe, M.W. Barsoum, Y. Gogotsi, *J. Mater. Chem. A* 2 (2014) 14334.
- [36] Y. Gao, L. Wang, A. Zhou, Z. Li, J. Chen, H. Bala, Q. Hu, X. Cao, *Mater. Lett.* 150 (2015) 62–64.
- [37] C. Peng, X. Yang, Y. Li, H. Yu, H. Wang, F. Peng, *ACS Appl. Mater. Interfaces* 8 (2016) 6051–6060.
- [38] H. Wang, R. Peng, Z.D. Hood, M. Naguib, S.P. Adhikari, Z. Wu, *ChemSusChem* 9 (2016) 1490–1497.
- [39] C. Peng, H. Wang, H. Yu, F. Peng, *Mater. Res. Bull.* 89 (2017) 16–25.
- [40] C.H. Lai, M.Y. Lu, L.J. Chen, *J. Mater. Chem.* 22 (2012) 19–30.
- [41] F. Zhang, S.S. Wong, *Chem. Mater.* 21 (2009) 4541–4554.
- [42] H. Kisch, *Acc. Chem. Res.* 50 (2017) 1002–1010.
- [43] W. Gao, W. Liu, Y. Leng, X. Wang, X. Wang, B. Hu, D. Yu, Y. Sang, H. Liu, *Appl. Catal. B Environ.* 176 (2015) 83–90.
- [44] J. Li, Y. Ma, Z. Ye, M. Zhou, H. Wang, C. Ma, D. Wang, P. Huo, Y. Yan, *Appl. Catal. B Environ.* 204 (2017) 224–238.
- [45] H. Wang, X. Yuan, Y. Wu, G. Zeng, H. Dong, X. Chen, L. Leng, Z. Wu, L. Peng, *Appl. Catal. B Environ.* 186 (2016) 19–29.
- [46] X. Zhao, H. Li, J. Zhang, L. Shi, D. Zhang, *Int. J. Hydrogen Energy* 41 (2016) 2447–2456.
- [47] W. Zhao, Y. Liu, Z. Wei, S. Yang, H. He, C. Sun, *Appl. Catal. B Environ.* 185 (2016) 242–252.
- [48] L. Zhang, D. Zhang, J. Zhang, S. Cai, C. Fang, L. Huang, H. Li, R. Gao, L. Shi, *Nanoscale* 5 (2013) 9821–9829.
- [49] J. Liu, J. Liu, Z. Zhao, Y. Wei, W. Song, J. Li, X. Zhang, *Ind. Eng. Chem. Res.* 56 (2017) 5833–5842.
- [50] S. Cai, H. Hu, H. Li, L. Shi, D. Zhang, *Nanoscale* 8 (2016) 3588–3598.
- [51] M. Naguib, M. Kurtoglu, V. Presser, J. Lu, J. Niu, M. Heon, L. Hultman, Y. Gogotsi, M.W. Barsoum, *Adv. Mater.* 23 (2011) 4248–4253.
- [52] X. Zhao, M. Liu, Y. Chen, B. Hou, N. Zhang, B. Chen, N. Yang, K. Chen, J. Li, L. An, J. Mater. Chem. A 3 (2015) 7870–7876.
- [53] J. Luo, W. Zhang, H. Yuan, C. Jin, L. Zhang, H. Huang, C. Liang, Y. Xia, J. Zhang, Y. Gan, X. Tao, *ACS Nano* 11 (2017) 2459–2469.
- [54] M.Q. Yang, B. Weng, Y.J. Xu, *Langmuir* 29 (2013) 10549–10558.
- [55] X. Qian, J. Ding, J. Zhang, Y. Zhang, Y. Wang, E. Kan, X. Wang, J. Zhu, *Nanoscale* 10 (2018) 1766–1773.
- [56] Y. Wang, H. Dou, J. Wang, B. Ding, Y. Xu, Z. Chang, X. Hao, *J. Power Sources* 327 (2016) 221–228.
- [57] J. Yan, C.E. Ren, K. Maleski, C.B. Hatter, B. Anasori, P. Urbankowski, A. Sarycheva, Y. Gogotsi, *Adv. Funct. Mater.* 27 (2017), <http://dx.doi.org/10.1002/adfm.201701264> 1701264.

- [58] M.D. Levi, M.R. Lukatskaya, S. Sigalov, M. Beidaghi, N. Shpigel, L. Daikhin, D. Aurbach, M.W. Barsoum, Y. Gogotsi, *Adv. Energy Mater.* 5 (2015) 1400815.
- [59] Y. Tang, J. Zhu, C. Yang, F. Wang, *J. Electrochem. Soc.* 163 (2016) A1975–A1982.
- [60] G. Li, L. Tan, Y. Zhang, B. Wu, L. Li, *Langmuir* 33 (2017) 9000–9006.
- [61] S. He, W. Chen, *J. Power Sources* 262 (2014) 391–400.
- [62] M. Naguib, O. Mashtalar, M.R. Lukatskaya, B. Dyatkin, C. Zhang, V. Presser, Y. Gogotsi, M.W. Barsoum, *Chem. Commun.* 50 (2014) 7420–7423.
- [63] H. Ghassemi, W. Harlow, O. Mashtalar, M. Beidaghi, M.R. Lukatskaya, Y. Gogotsi, M.L. Taheri, *J. Mater. Chem. A* 2 (2014) 14339.
- [64] H. Wang, X. Yuan, Y. Wu, G. Zeng, W. Tu, C. Sheng, Y. Deng, F. Chen, J.W. Chew, *Appl. Catal. B Environ.* 209 (2017) 543–553.
- [65] H. Wang, X. Yuan, Y. Wu, G. Zeng, X. Chen, L. Leng, H. Li, *Appl. Catal. B Environ.* 174–175 (2015) 445–454.
- [66] F.-X. Deng, J.-X. Yang, Y.-S. Zhu, F. Ma, S. Qiu, *Environ. Prog. Sustain. Energy* 37 (2017) 686–694, <http://dx.doi.org/10.1002/ep.12738>.
- [67] M.U.D. Sheikh, G.A. Naikoo, M. Thomas, M. Bano, F. Khan, *New J. Chem.* 40 (2016) 5483–5494.
- [68] T. Chen, Y. Zheng, J.-M. Lin, G. Chen, *J. Am. Soc. Mass Spectrom.* 19 (2008) 997–1003.
- [69] M. Sun, D. Li, Y. Chen, W. Chen, W. Li, Y. He, X. Fu, *J. Phys. Chem. C* 113 (2009) 13825–13831.
- [70] S. Tominaka, H. Yoshikawa, Y. Matsushita, A.K. Cheetham, *Mater. Horiz.* 1 (2014) 106–110.
- [71] H. Lee, S.J. Han, R. Chidambaram Seshadri, S. Sampath, *Sci. Rep.* 6 (2016) 36581.
- [72] J. Ma, H. Wu, Y. Liu, H. He, *J. Phys. Chem. C* 118 (2014) 7434–7441.
- [73] M. Khazaei, M. Arai, T. Sasaki, A. Ranjbar, Y.Y. Liang, S. Yunoki, *Phys. Rev. B* 92 (2015) 10.
- [74] S.M. Song, J.K. Park, O.J. Sul, B.J. Cho, *Nano Lett.* 12 (2012) 3887–3892.
- [75] M. Shiraishi, M. Ata, *Carbon* 39 (2001) 1913–1917.
- [76] S.Y. Lee, U.J. Kim, J. Chung, H. Nam, H.Y. Jeong, G.H. Han, H. Kim, H.M. Oh, H. Lee, H. Kim, Y.-G. Roh, J. Kim, S.W. Hwang, Y. Park, Y.H. Lee, *ACS Nano* 10 (2016) 6100–6107.
- [77] Z.Y. Zhao, Z.S. Li, Z.G. Zou, *J. Phys. Condens. Matter* 22 (2010).
- [78] E. Romero, V.I. Novoderezhkin, R. van Grondelle, *Nature* 543 (2017) 355–365.
- [79] H.A. Tahini, X. Tan, S.C. Smith, *Nanoscale* 9 (2017) 7016–7020.
- [80] Z.-F. Huang, J. Song, X. Wang, L. Pan, K. Li, X. Zhang, L. Wang, J.-J. Zou, *Nano Energy* 40 (2017) 308–316.
- [81] M. Jakob, H. Levanon, P.V. Kamat, *Nano Lett.* 3 (2003) 353–358.
- [82] C.C. Chen, W.H. Ma, J.C. Zhao, *Chem. Soc. Rev.* 39 (2010) 4206–4219.
- [83] X. Zhang, X. Li, C. Shao, J. Li, M. Zhang, P. Zhang, K. Wang, N. Lu, Y. Liu, J. Hazard. Mater. 260 (2013) 892–900.
- [84] John F. Callan, F.M. Raymo, (2012) Pan Stanford Publishing Pte. Ltd., DOI: 10.4032/9789814364614.
- [85] A. Di Paola, M. Bellardita, L. Palmisano, *Catalysts* 3 (2013) 36–73.
- [86] Y. Xie, P.R.C. Kent, *Phys. Rev. B* 87 (2013) 235441.
- [87] T. Su, R. Peng, Z.D. Hood, M. Naguib, I.N. Ivanov, J.K. Keum, Z. Qin, Z. Guo, Z. Wu, *ChemSusChem* 11 (2018) 688–699.
- [88] T. Hu, H. Zhang, J. Wang, Z. Li, M. Hu, J. Tan, P. Hou, F. Li, X. Wang, *Sci. Rep.* 5 (2015) 16329.